DOI: 10.19884/j.1672-5220.202503029

# Covalent Organic Framework with Electron Push-Pull Effect for Selective Photocatalytic Oxidation of Sulfides

HUANG Zhenxuan, ZHAO Qixin, JIANG Zhiqiang, ZENG Yang, SHEN Jiefeng*, XUAN Weimin*
State Key Laboratory of Advanced Fiber Materials, College of Chemistry and Chemical Engineering, Donghua University, Shanghai 201620, China

**Abstract: The selective aerobic oxidation of sulfides enables efficient production of sulfoxide-containing pharmaceuticals and agrochemicals. However, conventional catalytic systems frequently suffer from compromised selectivity due to undesired over-oxidation of sulfides to sulfones. Photocatalysis has emerged as a transformative strategy to address this persistent selectivity challenge, prompting extensive exploration of photocatalytic materials. In particular, covalent organic frameworks (COFs) distinguish themselves as superior platforms for the photocatalytic selective aerobic oxidation of sulfides, due to their structural tunability, tailorable optoelectronic properties, and operational durability under photocatalytic conditions. Herein, two COFs (TP-BPDA and BTT-BPDA) were synthesized via Schiff-base condensation. Photoelectrochemical experiments demonstrated that TP-BPDA, benefiting from a more pronounced electron push-pull effect, showed better photocatalytic performance for the selective aerobic oxidation of sulfides to sulfoxides. Moreover, TP-BPDA exhibited broad substrate generality. Based on the scavenger experiment, a putative reaction mechanism was proposed. This study provides guidance for the further development of high-efficiency photocatalysts for selective aerobic oxidation by leveraging the electron push-pull effect.**

**Keywords**: covalent organic framework; Schiff-base condensation; sulfoxide; photocatalysis
**CLC number**: O643.36 **Document code**: A
**Article ID**: 1672-5220(2026)05-0014-12

## 0 Introduction

The selective aerobic oxidation of sulfides to sulfoxides is a pivotal transformation in organic synthesis, with significant implications for constructing high-value fine chemicals, bioactive pharmaceuticals, and agrochemical intermediates[1-3]. Moreover, this process offers a promising strategy for reducing sulfur-containing organic fuels[4-10]. However, traditional catalytic methods often face challenges related to over-oxidation of sulfides to sulfones, which reduces product selectivity. Recent advances in photocatalysis have provided a sustainable solution to this persistent selectivity issue[11-13]. Photocatalysis, as an environmentally friendly methodology, utilizes light energy to drive chemical transformations, garnering significant research interest. While various photocatalytic materials, such as metal oxides[14-15], carbon-based nanomaterials[16], polyoxometalates[17-18], quantum dots[19], MXenes[20], and graphitic carbon nitride[21], have been explored, their practical applications are hindered by inherent limitations. Key challenges include inefficient light harvesting, poor material dispersion, limited functional tunability, inadequate selectivity, and environmental concerns associated with metal leaching. These issues highlight the urgent need for the development of advanced photocatalysts.

Covalent organic frameworks (COFs) are a novel class of organic porous materials, formed by linking organic building blocks through covalent bonds to create ordered and crystalline structures with tailored pores[22-23]. COFs have emerged as promising photocatalytic materials, offering distinct advantages over other photocatalyst systems[24-31]. Their extended conjugated systems enable superior light absorption across broad spectral ranges, while their periodic crystalline architectures facilitate efficient charge carrier separation and migration via well-defined electron transport pathways[32-34]. The high specific surface area of COFs provides abundant active sites, promoting substrate/product diffusion and facilitating the reaction. Moreover, the facile introduction of photoactive functionalities, achieved via organic building block design, imparts COFs with tunable photocatalytic activities[35-39]. Furthermore, the chemical and thermal stability of COFs ensures operational durability under demanding reaction

Received date: 2025-03-28
Foundation items: National Natural Science Foundation of China (Nos. 92161111, 21901038, and 22071148); the Program for Professor of Special Appointment (Eastern Scholar) at Shanghai Institutions of Higher Learning; International Cooperation Fund of Science and Technology Commission of Shanghai Municipality, China (No. 21130750100); Fundamental Research Funds for the Central Universities, China (No. 2232023A-07)
* Correspondence should be addressed to SHEN Jiefeng, email: jiefeng@dhu.edu.cn; XUAN Weimin, email: weiminxuan@dhu.edu.cn
Citation: Huang Z X, Zhao Q X, Jiang Z Q, et al. Covalent organic framework with electron push-pull effect for selective photocatalytic oxidation of sulfides [J]. *Journal of Donghua University (English Edition)*, 2026, 43(5): 14-25.

conditions. This unique combination of all these advantages renders COFs ideal candidates to overcome the limitations of traditional photocatalysts[40-43].

In this study, we synthesized two COFs using the photosensitive building block, $N^4$,$N^4$-bis(4′-amino-[1,1′-biphenyl]-4-yl)-[1,1′-biphenyl]-4,4′-diamine (BPDA), together with two different aldehyde monomers: 2,4,6-triformylphloroglucinol (TP) and benzo[1,2-b:3,4-b′:5,6-b″] trithiophene-2,5,8-tricarbaldehyde (BTT). The resulting COFs are denoted TP-BPDA and BTT-BPDA, respectively. We systematically investigated their photocatalytic performance in the selective oxidation of sulfides. Photoelectrochemical characterizations, radical-scavenging tests, control experiments, and electron paramagnetic resonance (EPR) measurements were employed to reveal the structure-property relationship and to gain insight into the reaction mechanism. This work is expected to pave the way for exploration of novel COF-based photocatalysts for the selective aerobic oxidation of sulfides.

# 1 Experimental Section

## 1.1 Materials and methods

Butyl alcohol (*n*-BuOH), acetic acid, acetone, 1,2-dichlorobenzene (*o*-DCB), ether, tetrahydrofuran, methanol, and various sulfide substrates were purchased from General Reagent Co., Ltd., Shanghai, China. BPDA, TP, and BTT were purchased from Bidepharm Co., Ltd., Shanghai, China. All commercially available materials were analytically pure reagents and used as received without further purification.

Powder X-ray diffraction (PXRD) was performed to test the crystallinity of COFs using a powder diffractometer (D2 PHASER, Bruker Corporation, Germany) equipped with a copper target, with a scanning angle ranging from 3° to 30° and a scanning speed of 5 (°)/min. The Fourier transform infrared (FTIR) spectroscopy was performed on an FTIR spectrometer (iS50, Thermo Fisher Scientific, USA) in the range of 400 to 4 000 $cm^{-1}$. The solid-state $^{13}C$ nuclear magnetic resonance (NMR) was performed on an NMR spectrometer (AVANCE Ⅲ HD 600, Bruker Corporation, Germany). Nitrogen adsorption and desorption measurements were performed using a fully automated physical adsorbent apparatus (ASAP 2460, Micromeritics Instrument Corporation, USA) at −196 ℃ under liquid nitrogen cooling. The specific surface area of COFs was analyzed by the Brunauer-Emmett-Teller (BET) method. Thermogravimetric analysis (TGA) was performed using a thermogravimetric analyzer (TGA 8000, PerkinElmer, USA) under nitrogen flow at a heating rate of 10 ℃/min, from 30 to 800 ℃. The structures of COFs were simulated using the Materials Studio 2019 software and optimized using the Forcite module, and the final refinement was further carried out using the Pawley module to obtain an optimal structural model. Simulations and analyses of the electrostatic potential (ESP) of the structural units of COFs were carried out using the DMol$^3$ module.

The photocatalytic oxidation was carried out at room temperature by adding 0.3 mmol sulfide and 5 mg catalyst to 1 mL methanol in a 20 mL quartz tube equipped with a magnetic stir bar. The reaction was then stirred under irradiation from a 10 W, 420 nm light-emitting diode (LED) lamp. At the end of the reaction, the mixture was centrifuged and filtered, and the reaction yield was determined on a gas chromatograph-mass spectrometer (GC-MS 7890B-5977B, Agilent Technologies, USA).

## 1.2 Synthesis of COFs

TP-BPDA or BTT-BPDA was synthesized as follows. BPDA (0.1 mmol) and TP (0.1 mmol) or BTT (0.1 mmol) were added to a 10 mL glass vial. Subsequently, 0.25 mL *n*-BuOH and 0.75 mL *o*-DCB were added. After sonication of the monomer solution for 15 min, the mixture was transferred to a quartz tube, to which 0.1 mL of 6 mol/L acetic acid was slowly added. The quartz tube was attached to the vacuum sealer for vacuum/nitrogen cooling. Then, it was sealed with a flame gun under vacuum. After returning to room temperature, it was heated at 120 ℃ and kept for 72 h, and then cooled to room temperature. The dark red solid, obtained by filtration and washed three times with acetone and ether successively, was Soxhlet-extracted with tetrahydrofuran and acetone for 24 h each, and then vacuum-dried overnight at 80 ℃. The schematic representation of the synthesis and structures of TP-BPDA and BTT-BPDA is shown in Fig. 1.

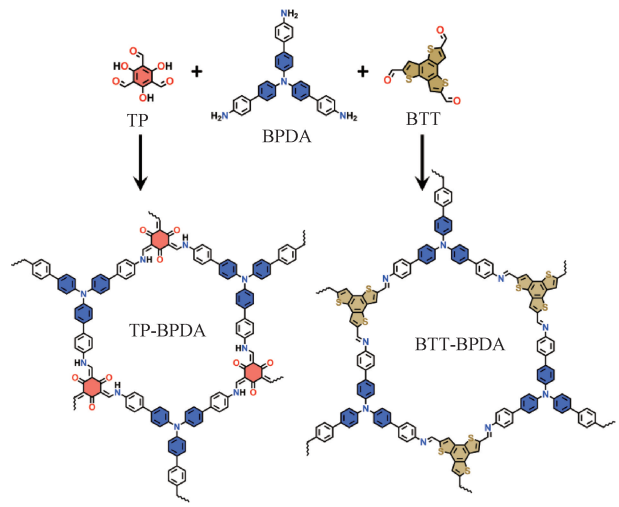



Fig. 1 Schematic representation of synthesis and structures of TP-BPDA and BTT-BPDA

# 2 Results and Discussion

## 2.1 Crystal structure determination

The structures of TP-BPDA and BTT-BPDA were characterized by PXRD and analyzed through theoretical structural simulations. As shown in Figs. 2(a) and

2(b), both TP-BPDA and BTT-BPDA exhibit similar strong diffraction peaks, revealing their high crystallinity and isoreticular structures. Based on the geometric features and connection directions of TP, BTT, and BPDA, three possible stacking models (AA, AB, and ABC stacking, representing eclipsed, two-layer staggered, and three-layer staggered arrangements, respectively) were built using the Materials Studio 2019 software. Among these models, the eclipsed AA stacking configuration closely matches most of the diffraction peaks observed in the refined PXRD pattern of TP-BPDA and BTT-BPDA, in terms of both position and intensity. The experimental diffraction peaks observed at $2\theta$ values of 4.6°, 7.7°, 8.9° and 11.7° for TP-BPDA and 3.8°, 6.6°, 7.6° and 10.0° for BTT-BPDA can be assigned to the (110), (300), (220) and (140) reflection planes, respectively.

Further refinement of the structures using the Pawley module produced negligible deviations, confirming the validity of the computational models, with $R_{wp}$ = 2.10% and $R_p$ = 1.60% for TP-BPDA (Fig. 2(c)) and $R_{wp}$ = 8.28% and $R_p$ = 6.34% for BTT-BPDA (Fig. 2(e)). Here, $R_{wp}$ and $R_p$ correspond to the weighted residual factor and the residual factor, respectively. The cell parameters associated with stacking model structures are determined: $a=b$=41.07 Å (1 Å=0.1 nm), $c$=3.62 Å for TP-BPDA, and $a=b$=46.98 Å, $c$=3.63 Å for BTT-BPDA (Figs. 2(d) and 2(f)).

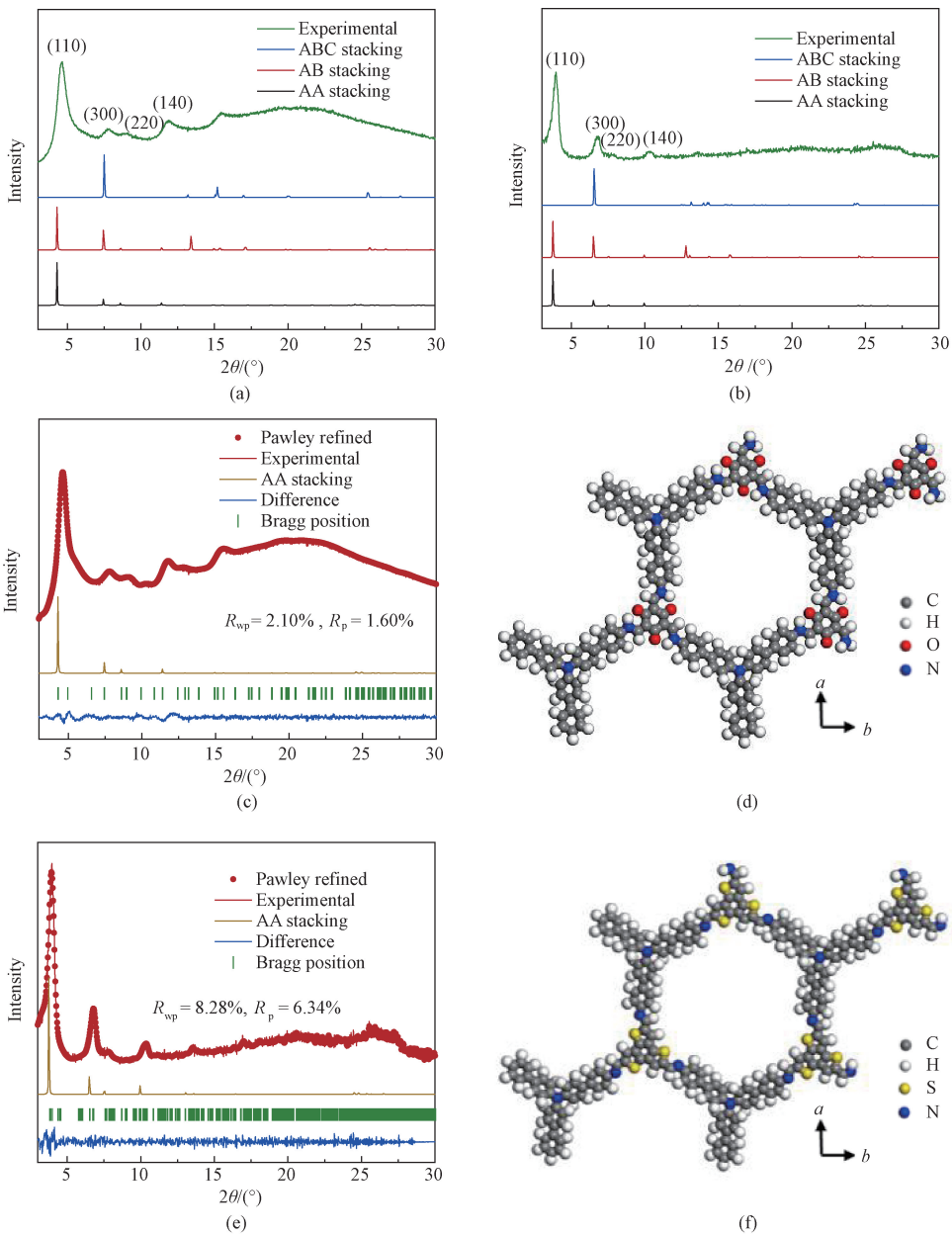



Fig. 2 PXRD analysis: (a) comparison of experimental PXRD pattern of TP-BPDA with simulated patterns; (b) comparison of experimental PXRD pattern of BTT-BPDA with simulated patterns; (c) refined PXRD patterns of TP-BPDA; (d) stacking model structure of TP-BPDA; (e) refined PXRD patterns of BTT-BPDA; (f) stacking model structure of BTT-BPDA

## 2.2 Spectral characterization and porosity study

To further investigate the structures of COFs, FTIR, solid-state $^{13}C$ NMR, and $N_2$ adsorption-desorption tests were performed. The FTIR spectrum of TP-BPDA shows characteristic C—N and C═O stretching vibration peaks at 1 281 and 1 597 $cm^{-1}$, respectively, while that of BTT-BPDA exhibits a characteristic C═N stretching vibration peak at 1 599 $cm^{-1}$ (Figs. 3(a) and 3(b)). Meanwhile, the C═O stretching bands in TP (1 637 $cm^{-1}$) and BTT (1 660 $cm^{-1}$) almost disappear (Figs. 3(a) and 3(b)), indicating that the aldehyde and amino precursors undergo a Schiff-base condensation and successfully form imine bonds.

The solid-state $^{13}C$ NMR spectra of TP-BPDA and BTT-BPDA are shown in Figs. 3(c) and 3(d), respectively. The analysis reveals that the prominent peaks at chemical shifts of 182 and 146 in the spectrum of TP-BPDA correspond to the resonances of ketone-type carbon and C═C—N carbon, respectively. The prominent peak at a chemical shift of 146 in the spectrum of BTT-BPDA is characteristic of C═N carbon. The presence of these signals indicates the formation of imine bonds and confirms the successful synthesis of COFs.

The specific surface areas and permanent porosities of TP-BPDA and BTT-BPDA were assessed via $N_2$ adsorption-desorption. As shown in Figs. 3(e) and 3(f), the rapid $N_2$ adsorption at low relative pressure indicates that both TP-BPDA and BTT-BPDA possess typical microporous characteristics. Here, $P/P_0$ denotes the relative pressure, while $dV/dD$ refers to the differential pore size distribution. Moreover, based on the $N_2$ adsorption-desorption isotherms and the BET model, the specific surface areas of TP-BPDA and BTT-BPDA were calculated to be 527.19 and 416.36 $m^2/g$, respectively. The pore size distributions, determined by the non-local density functional theory (NLDFT) model, reveal average pore sizes of approximately 1.1 nm for TP-BPDA and 1.3 nm for BTT-BPDA.

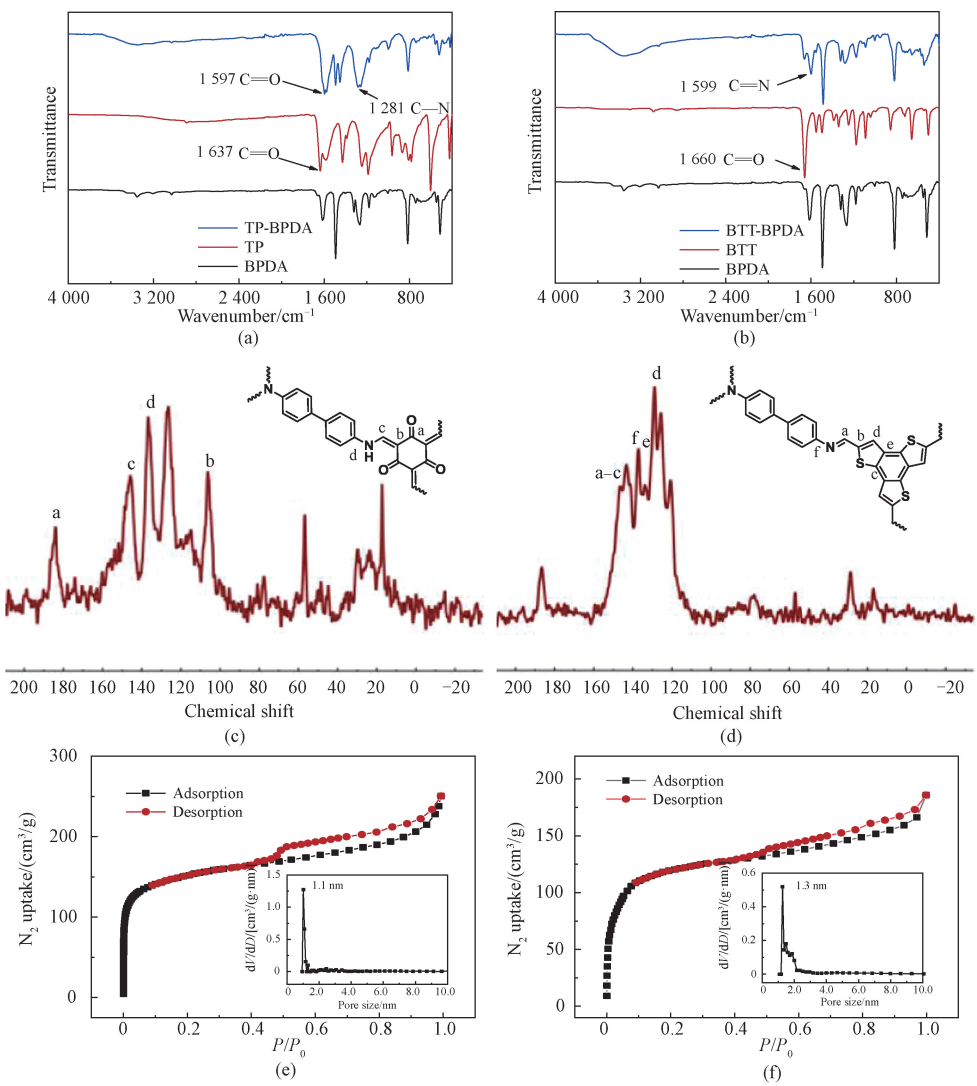



Fig. 3 Spectral characterization and porosity study of COFs: (a) FTIR spectra of TP-BPDA and corresponding precursors; (b) FTIR spectra of BTT-BPDA and corresponding precursors; (c) solid-state $^{13}C$ NMR spectrum of TP-BPDA; (d) solid-state $^{13}C$ NMR spectrum of BTT-BPDA; (e) $N_2$ adsorption-desorption isotherms and pore size distributions of TP-BPDA; (f) $N_2$ adsorption-desorption isotherms and pore size distributions of BTT-BPDA

### 2.3 ESP calculation and thermal stability analysis

ESP maps were used to investigate the orbital electron distributions of the two COFs, as depicted in Figs. 4(a) and 4(b). The ESP map of TP-BPDA reveals that the maximum negative charge (indicated by red regions) is concentrated on the O atoms within the TP structural unit. In contrast, the maximum negative charge in BTT-BPDA is centered on the N atoms. This distribution demonstrates that the TP building block possesses a stronger electron-withdrawing ability, resulting in a more pronounced electron push-pull effect in TP-BPDA than in BTT-BPDA.

As shown in Figs. 4(c) and 4(d), TP-BPDA and BTT-BPDA show good thermal stability up to 300 ℃, with total mass losses of 13.1% and 15.1%, respectively, which can be attributed to residual guest or solvent molecules located in the one-dimensional (1D) open channels.

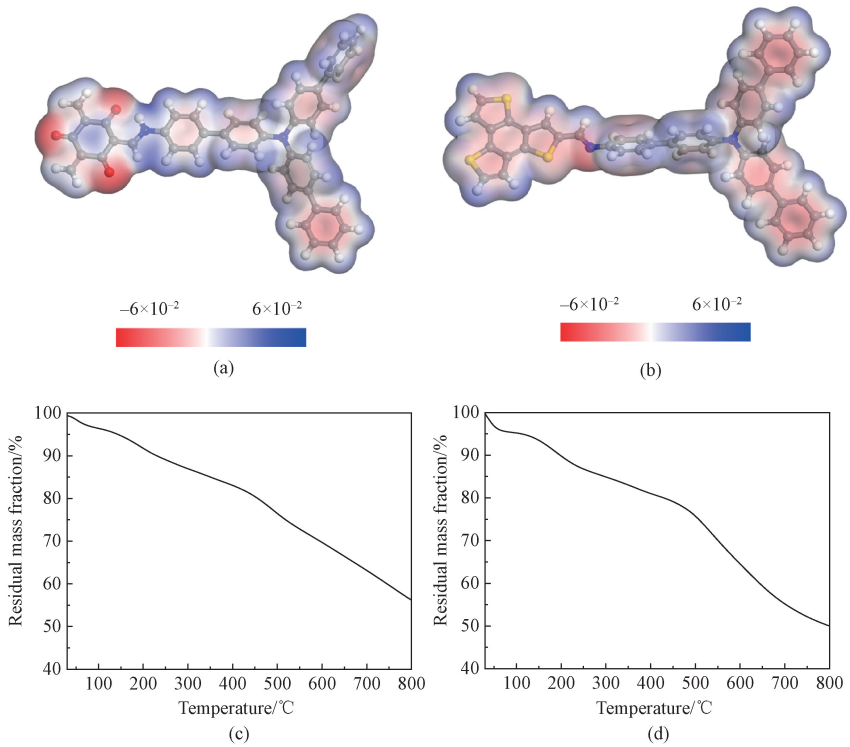



Fig. 4 ESP maps and TGA curves of COFs: (a) ESP map of TP-BPDA; (b) ESP map of BTT-BPDA; (c) TGA curve of TP-BPDA; (d) TGA curve of BTT-BPDA

### 2.4 Photoelectrochemical characterization

The solid state ultraviolet-visible diffuse reflectance spectra (UV-vis DRS) were recorded to evaluate the absorption features of TP-BPDA and BTT-BPDA (Fig. 5(a)). Both structures display a very broad absorption band ranging from 300 to 600 nm. The band gaps of TP-BPDA and BTT-BPDA, determined by analyzing the absorption coefficient $\alpha$, Planck's constant $h$, and optical frequency $v$ from Tauc plots, are 1.88 and 2.10 eV, respectively (Fig. 5(b)). Benefiting from the strong electron-withdrawing ability of the TP unit, TP-BPDA exhibits a more pronounced electron push-pull effect than BTT-BPDA, which enhances its photogenerated charge separation ability. This trend is reflected in Fig. 5(c), where TP-BPDA shows a higher photocurrent intensity than BTT-BPDA, indicating more efficient charge carrier generation and separation under light irradiation. Accordingly, TP-BPDA also exhibits a smaller Nyquist semicircle radius than BTT-BPDA, as evidenced by the Nyquist plots of electrochemical impedance spectroscopy (EIS) (Fig. 5(d)). In Fig. 5(d), $Z'$ and $Z''$ represent the real and imaginary parts of the alternating current impedance, respectively. This lower resistance facilitates the rapid transfer of charge carriers, which is crucial for enhancing the photocatalytic performance.

To gain deeper insights into the electronic properties of these two COFs, Mott-Schottky analysis was performed at three different frequencies. The space-charge-layer capacitance $C$ was analyzed using the relevant equation, with the values expressed in farads (F). The analysis shows that the flat band potentials of TP-BPDA and BTT-BPDA with respect to Ag/AgCl are −0.61 and −0.69 V, respectively (Figs. 5(e) and 5(f)). These potentials are sufficiently negative to drive the activation of $O_2$ to superoxide radical ($O_2^{\cdot-}$), a key reactive oxygen species in photocatalytic reactions. Therefore, the combination of broad light absorption, favorable band gaps, efficient charge separation, and suitable flat band potentials makes these two COFs promising candidates for photocatalytic selective oxidation.

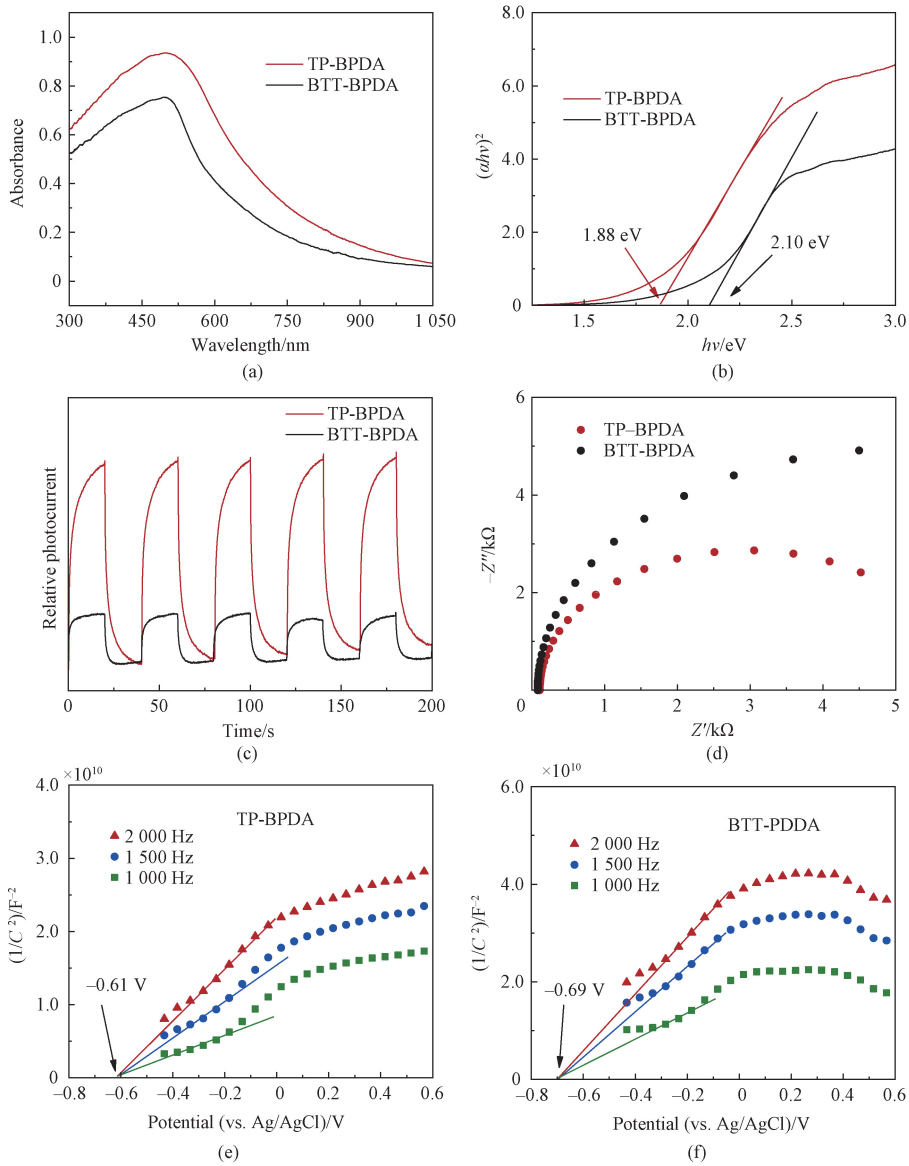



Fig. 5 Photoelectrochemical characterization: (a) solid-state UV-vis DRS of TP-BPDA and BTT-BPDA; (b) Tauc plots of TP-BPDA and BTT-BPDA; (c) photocurrent-time curves of TP-BPDA and BTT-BPDA; (d) EIS Nyquist plots of TP-BPDA and BTT-BPDA; (e) Mott-Schottky plots of TP-BPDA; (f) Mott-Schottky plots of BTT-BPDA

## 2.5 Photocatalytic oxidation of sulfides

The photocatalytic activities of these two COFs toward selective aerobic oxidation of sulfides were evaluated using methyl phenyl sulfide as a model substrate. The optimal reaction conditions were identified with 0.3 mmol methyl phenyl sulfide, 5 mg COFs, and 1 mL $CH_3OH$ as the solvent under 420 nm blue-light irradiation and an $O_2$ atmosphere of $1.01\times10^5$ Pa for a reaction time of 1 h. TP-BPDA affords a higher sulfoxide yield than BTT-BPDA (Fig. 6(a)). The superior photocatalytic activity of TP-BPDA is further confirmed using sulfide substrates bearing either electron-withdrawing or electron-donating groups, both of which are converted into corresponding sulfoxides with significantly higher efficiency (Fig. 6(a)). This fully demonstrates that the stronger electron push-pull effect induced by the TP unit positively enhances the photocatalytic performance, which correlates with the photocurrent sequence for TP-BPDA and BTT-BPDA (Fig. 5(c)).

Next, a series of solvents were screened. The highest conversion is achieved when methanol is used as the solvent (Fig. 6(b)). To better understand the reactive species responsible for the photocatalytic oxidation and elucidate the reaction mechanism, a series of scavenger and control experiments were performed. Results are shown in Fig. 6(c). It is noteworthy that the oxidation of methyl phenyl sulfide hardly proceeds under an inert $N_2$ atmosphere, whereas the yield decreases markedly under an air atmosphere, indicating the essential role of $O_2$ for the reaction. The conversion is

hardly detectable in the absence of light irradiation, revealing the light-driven nature of photocatalysis. Subsequently, different quenchers were added to identify the possible reactive oxygen species (ROSs) involved during oxidation. The introduction of KI and $AgNO_3$ as scavengers for photogenerated holes ($h^+$) and electrons ($e^-$) results in a dramatic decrease in sulfide conversion, implying that both $h^+$ and $e^-$ play decisive roles in activating substrates and producing ROS. The oxidation of methyl phenyl sulfide is greatly inhibited by the addition of *p*-benzoquinone (*p*-BQ) as a scavenger for $O_2^{\cdot -}$, suggesting that $O_2^{\cdot -}$ has a significant influence during the reaction process. When 1,4-diazabicyclo [2.2.2] octane (DABCO) is added to the system as a scavenger for $^1O_2$, the yield shows an obvious decrease, indicating that $^1O_2$ also contributes to the formation of the sulfoxide product. The generation of $O_2^{\cdot -}$ during selective aerobic oxidation is confirmed by the presence of characteristic EPR signals according to the 5,5-dimethyl-1-pyrroline *N*-oxide (DMPO)-$O_2^{\cdot -}$ adduct. However, no EPR signals corresponding to $^1O_2$ are observed in the presence of 2,2,6,6-tetramethylpiperidine (TEMP) under identical experimental conditions (Fig. 6(d)). Furthermore, the photocatalytic oxidation yields of TP-BPDA at different irradiation powers were compared. As shown in Fig. 6(e), as the irradiation power increases, the photocatalytic oxidation yield increases accordingly. To determine the stability of TP-BPDA after the reaction, the PXRD patterns of TP-BPDA before and after the reaction are compared. As shown in Fig. 6(f), the PXRD patterns of TP-BPDA show little change, demonstrating its stability.

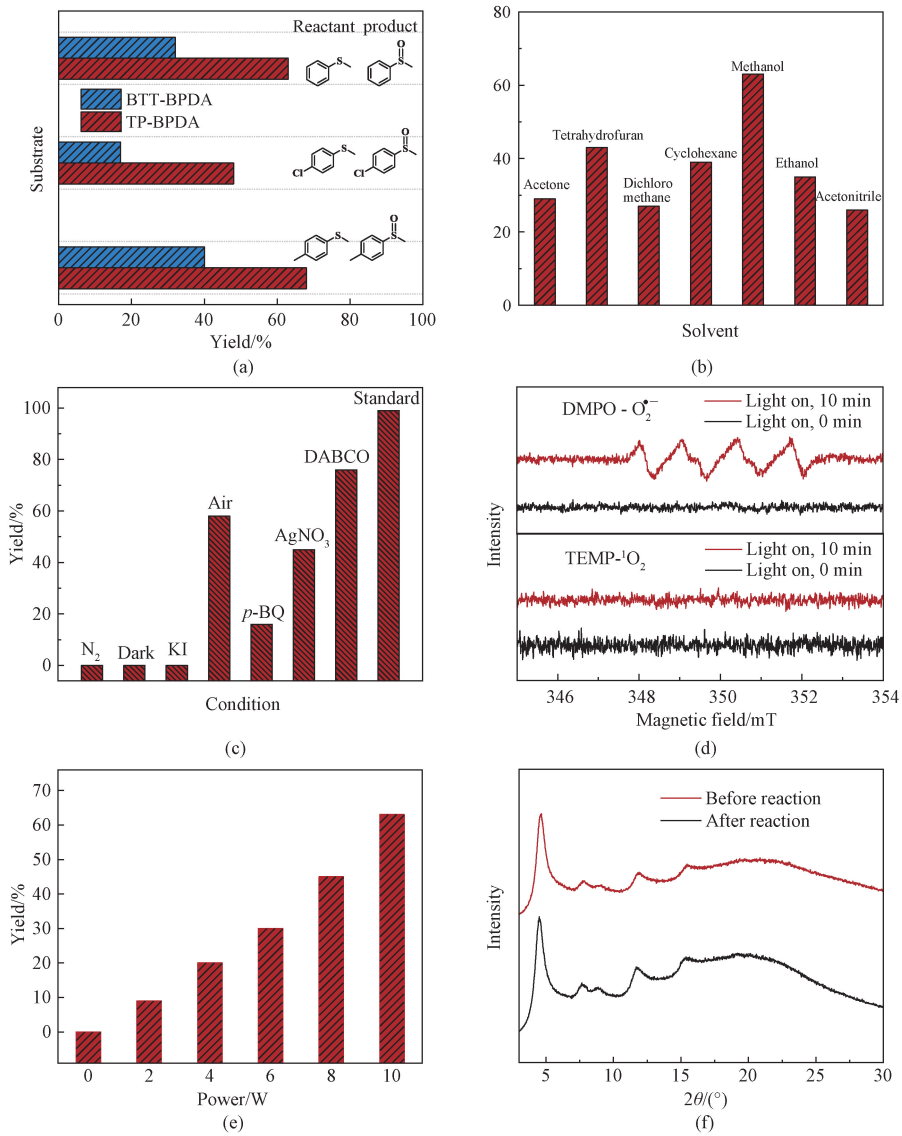



Fig. 6 Photocatalytic oxidation study of COFs: (a) comparison of TP-BPDA with BTT-BPDA in selective aerobic oxidation of three sulfides; (b) reaction yields of TP-BPDA under different solvents; (c) scavenger and control experiments; (d) EPR detection of evolution of $O_2^{\cdot -}$ and $^1O_2$ probed by TP-BPDA; (e) reaction yields of TP-BPDA under different irradiation powers; (f) PXRD patterns of TP-BPDA before and after reaction

Based on the results of scavenger and control experiments, as well as EPR data, we proposed a possible mechanism for TP-BPDA photocatalysis (Fig. 7). Initially, under the blue light irradiation, TP-BPDA was activated, and the photogenerated $e^-$ leapt from the highest occupied molecular orbital (HOMO) to the lowest unoccupied molecular orbital (LUMO), which were further captured by $O_2$ molecules to generate $O_2^{\cdot -}$. Meanwhile, the sulfide substrate was oxidized by $h^+$ to form a radical cation, which subsequently reacted with $O_2^{\cdot -}$ to produce a peroxide intermediate. Finally, the peroxide intermediate combined with another molecule of sulfide to form the sulfoxide product.

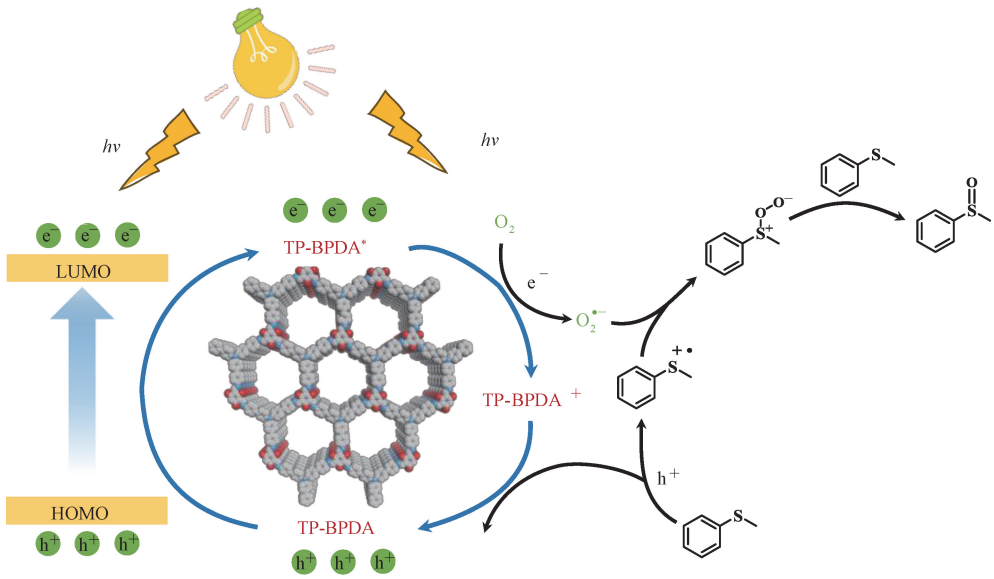



Fig. 7 Possible mechanism for blue-light-driven selective aerobic oxidation of sulfides by TP-BPDA

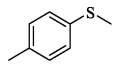
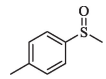
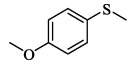
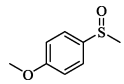
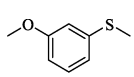
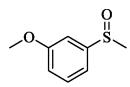
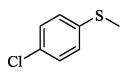
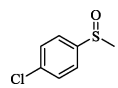
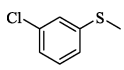
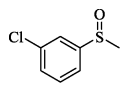
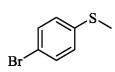
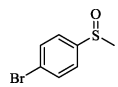
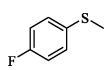
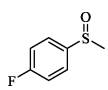
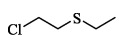
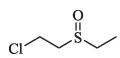
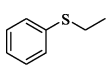
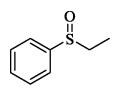
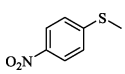
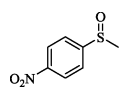
Various methyl phenyl sulfide derivatives were explored as substrates to examine the generality of TP-BPDA. The general reaction for this substrate-scope study is illustrated in Fig. 8, and the detailed results are summarized in Table 1. Both substrate conversion and sulfoxide product selectivity were determined by gas chromatography-mass spectrometry (GC-MS).




Fig. 8 General reaction for substrate-scope study

To our delight, TP-BPDA exhibits broad applicability toward photocatalytic selective aerobic oxidation, smoothly converting all tested sulfides and derivatives into corresponding sulfoxides with excellent conversion and selectivity. The electronic and steric effects of the substituents mainly affect the conversion rate of the sulfides. Specifically, sulfides with electron-donating groups exhibit high conversion (Table 1, entries 1 – 5). In contrast, sulfides with different electron-withdrawing groups show lower conversions to varying degrees (Table 1, entries 8 and 9). Moreover, a steric effect is also observed for Cl-substituted phenylmethyl sulfides, and the conversion decreases in the order of *para*, *meta*, and *ortho* positions (Table 1, entries 6–8). Additionally, sulfides such as 2-chloroethyl sulfide and phenylethyl sulfide can be successfully converted into the corresponding sulfoxides with high conversion (Table 1, entries 11 and 12). For the heterocyclic sulfide, 3-(methylthio) pyridine, a relatively low conversion is obtained due to the poisoning effect of the heteroatom (Table 1, entry 14). In summary, TP-BPDA acts as a versatile catalyst for the photocatalytic selective aerobic oxidation of sulfides.

**Table 1** Aerobic oxidation of sulfides by TP-BPDA photocatalysis

| Entry | Substrate | Product | Time/h | Conversion/% | Selectivity/% |
|---|---|---|---|---|---|
| 1 |  |  | 2.0 | 99 | 98 |
| 2 |  |  | 2.0 | 93 | 99 |
| 3 |  |  | 2.0 | 99 | 98 |
| 4 |  |  | 2.0 | 99 | 98 |
| 5 |  |  | 2.0 | 99 | 91 |
| 6 |  |  | 3.0 | 99 | 90 |
| 7 |  |  | 3.0 | 83 | 99 |
| 8 |  |  | 3.0 | 85 | 99 |
| 9 |  |  | 3.2 | 94 | 98 |
| 10 |  |  | 3.2 | 99 | 92 |
| 11 |  |  | 4.0 | 90 | 92 |
| 12 |  |  | 1.5 | 99 | 90 |
| 13 |  |  | 3.0 | 99 | 91 |
| 14 |  |  | 4.0 | 52 | 99 |

## 3 Conclusions

In conclusion, two photoactive COFs have been successfully constructed via Schiff-base condensation of BPDA with electron-donating BTT and electron-withdrawing TP units. Photoelectrochemical characterization demonstrates that TP-BPDA exhibits broader light-harvesting capacity, better charge separation efficiency, and a narrower band gap than BTT-BPDA, owing to the stronger electron push-pull effect. By leveraging these advantages, TP-BPDA demonstrates superior photocatalytic performance in the selective aerobic oxidation of sulfides, affording a variety of sulfoxides with high conversion and selectivity. Mechanism studies reveal that $O_2^{\cdot -}$ is the major ROS responsible for the oxidation, while $^1O_2$ also contributes to sulfoxide generation. This work provides an effective strategy for building COF-based photocatalysts for selective aerobic oxidative transformation by regulating the electron effect via the rational combination of functional organic building blocks.

## References


[1] Wojaczyńska E, Wojaczyński J. Sulfoxides in medicine [J]. *Current Opinion in Chemical Biology*, 2023, 76: 102340.

[2] McCaw P G, Buckley N M, Collins S G, et al. Generation, reactivity and uses of sulfines in organic synthesis [J]. *European Journal of Organic Chemistry*, 2016, 2016(9): 1630-1650.

[3] Han Y, Xing K, Zhang J, et al. Application of sulfoximines in medicinal chemistry from 2013 to 2020 [J]. *European Journal of Medicinal Chemistry*, 2021, 209: 112885.

[4] Zhou X Y, Wang T Y, Liu H, et al. Desulfurization through photocatalytic oxidation: a critical review [J]. *ChemSusChem*, 2021, 14(2): 492-511.

[5] Stanislaus A, Marafi A, Rana M S. Recent advances in the science and technology of ultra low sulfur diesel (ULSD) production [J]. *Catalysis Today*, 2010, 153(1/2): 1-68.

[6] Xie Q L, Cai L, Xia F, et al. High vacuum distillation for low-sulfur biodiesel production: from laboratory to large scale [J]. *Journal of Cleaner Production*, 2019, 223: 379-385.

[7] Ma H, Addy M M, Anderson E, et al. A novel process for low-sulfur biodiesel production from scum waste [J]. *Bioresource Technology*, 2016, 214: 826-835.

[8] Zou X N, Zhang D S, Luan T X, et al. Incorporating photochromic triphenylamine into a zirconium-organic framework for highly effective photocatalytic aerobic oxidation of sulfides [J]. *ACS Applied Materials & Interfaces*, 2021, 13(17): 20137-20144.

[9] Watanabe S, Takayama T, Nishio H, et al. Synthesis of colorless and high-refractive-index sulfoxide-containing polymers by the oxidation of poly(phenylene sulfide) derivatives [J]. *Polymer Chemistry*, 2022, 13(12): 1705-1711.

[10] Cetina-Mancilla E, Reyes-García G A, Rodríguez-Molina M, et al. Room temperature, simple and efficient synthesis and functionalization of aromatic poly(arylene sulfide)s, poly(arylene sulfoxide)s and poly(arylene sulfone)s [J]. *European Polymer Journal*, 2023, 184: 111800.

[11] Kowalski P, Mitka K, Ossowska K, et al. Oxidation of sulfides to sulfoxides: part 1: oxidation using halogen derivatives [J]. *Tetrahedron*, 2005, 61(8): 1933-1953.

[12] Su C L, Tandiana R, Tian B B, et al. Visible-light photocatalysis of aerobic oxidation reactions using carbazolic conjugated microporous polymers [J]. *ACS Catalysis*, 2016, 6(6): 3594-3599.

[13] Heydari-Turkmani A, Zakavi S. The first solid state porphyrin-weak acid molecular complex: a novel metal free, nanosized and porous photocatalyst for large scale aerobic oxidations in water [J]. *Journal of Catalysis*, 2018, 364: 394-405.

[14] Zhang Y M, Zhao Z Y, Tang W, et al. $CuCoO_2$/CuO heterostructure: understanding the role of band alignment in selective catalysis for overall water splitting [J]. *Journal of Materials Chemistry A*, 2023, 11(37): 20151-20164.

[15] Li Y L, Chen S H, Duan W Y, et al. Research progress of vanadium pentoxide photocatalytic materials [J]. *RSC Advances*, 2023, 13(33): 22945-22957.

[16] Lu K Q, Li Y H, Tang Z R, et al. Roles of graphene oxide in heterogeneous photocatalysis [J]. *ACS Materials Au*, 2021, 1(1): 37-54.

[17] Chen Y H, An H Y, Chang S Z, et al. Visible-light-responsive 2D photocatalysts assembled by Evans-Showell-type POMs and metalloviologen frameworks for sulfide-sulfoxide transformation [J]. *Inorganic Chemistry*, 2023, 62(26): 10120-10130.

[18] Zhou D X, Li B B, Zhao Q X, et al. Solvent-modulated assembly of peptide and cerium functionalized gigantic $\{Mo_{120}Ce_6\}_2$ dimers for high-efficiency photocatalytic oxidation [J]. *Inorganic Chemistry Frontiers*, 2024, 11(8): 2355-2364.

[19] Chakraborty I N, Roy P, Pillai P P. Visible light-mediated quantum dot photocatalysis enables olefination reactions at room temperature [J]. *ACS Catalysis*, 2023, 13(11): 7331-7338.

[20] Tang R D, Xiong S, Gong D X, et al. $Ti_3C_2$ 2D MXene: recent progress and perspectives in photocatalysis [J]. *ACS Applied Materials & Interfaces*, 2020, 12(51): 56663-56680.

[21] Liu S W, Xi C J, Zhang L P, et al. Modification of graphite carbon nitride by nitrogen-doping and in situ loading $CoSe_x$ as co-catalyst by light-assisted synthesis for enhanced photocatalytic hydrogen production [J]. *Journal of Donghua University (English Edition)*, 2024, 41(3): 249-256.

[22] Liu Y K, Liu X N, Su A, et al. Revolutionizing the structural design and determination of covalent-organic frameworks: principles, methods, and techniques [J]. *Chemical Society Reviews*, 2024, 53(1): 502-544.

[23] Huang T H, Zhang W F, Yang S, et al. Imine-linked covalent organic frameworks: recent advances in design, synthesis, and application [J]. *SmartMat*, 2024, 5(6): e1309.

[24] Pai N, Lu J F, Wang M C, et al. Enhancement of the intrinsic light harvesting capacity of $Cs_2AgBiBr_6$ double perovskite via modification with sulphide [J]. *Journal of Materials Chemistry*

*A*, 2020, 8(4): 2008-2020.
[25] Qin L Y, Ma C D, Zhang J, et al. Structural motifs in covalent organic frameworks for photocatalysis [J]. *Advanced Functional Materials*, 2024, 34(41): 2401562.
[26] Mishra B, Alam A, Chakraborty A, et al. Covalent organic frameworks for photocatalysis [J]. *Advanced Materials*, 2025, 37(52): 2413118.
[27] Hsueh C H, He C, Zhang J Q, et al. Three-dimensional mesoporous covalent organic framework for photocatalytic oxidative dehydrogenation to quinoline[J]. *Journal of the American Chemical Society*, 2024, 146(49): 33857-33864.
[28] Shen R C, Huang C, Hao L, et al. Ground-state charge transfer in single-molecule junctions covalent organic frameworks for boosting photocatalytic hydrogen evolution [J]. *Nature Communications*, 2025, 16(1): 2457.
[29] Xu Q, Han J W, Tian F K, et al. Synergistic bifunctional covalent organic framework for efficient photocatalytic $CO_2$ reduction and water oxidation[J]. *Journal of the American Chemical Society*, 2025, 147(12): 10587-10597.
[30] Lin W, Lin F W, Lin J, et al. Efficient photocatalytic $CO_2$ reduction in ellagic acid-based covalent organic frameworks[J]. *Journal of the American Chemical Society*, 2024, 146(23): 16229-16236.
[31] Luan T X, Xing L B, Lu N, et al. Donor-acceptor-π-acceptor-donor-type photosensitive covalent organic framework for effective photocatalytic aerobic oxidation[J]. *Journal of the American Chemical Society*, 2025, 147(15): 12704-12714.
[32] Chen Z S, Wang J Y, Hao M J, et al. Tuning excited state electronic structure and charge transport in covalent organic frameworks for enhanced photocatalytic performance[J]. *Nature Communications*, 2023, 14(1): 1106.
[33] Li Z F, Dong Z M, Zhang Z B, et al. Covalent organic frameworks for boosting $H_2O_2$ photosynthesis via the synergy of multiple charge transfer channels and polarized field [J]. *Angewandte Chemie International Edition*, 2025, 64(7): e202420218.
[34] Ma S, Li Z P, Hou Y X, et al. Fully conjugated benzobisoxazole-bridged covalent organic frameworks for boosting photocatalytic hydrogen evolution[J]. *Angewandte Chemie International Edition*, 2025, 64(19): e202501869.
[35] Wang L J, Dong P Y, Zhang G L, et al. Review and perspectives of β-keto-enamine-based covalent organic framework for photocatalytic hydrogen evolution[J]. *Energy & Fuels*, 2023, 37(9): 6323-6347.
[36] Mishra B, Alam A, Kumbhakar B, et al. Impact of the crystallinity of covalent organic frameworks on photocatalytic hydrogen evolution[J]. *Crystal Growth & Design*, 2023, 23(6): 4701-4719.
[37] Vignesh B H, Monika B M G, Rajeswara R M. Functional π-conjugated two-dimensional covalent organic frameworks[J]. *ACS Applied Materials & Interfaces*, 2019, 11(12): 11029-11060.
[38] Geng K Y, He T, Liu R Y, et al. Covalent organic frameworks: design, synthesis, and functions [J]. *Chemical Reviews*, 2020, 120(16): 8814-8933.
[39] Huang L J, Yang J, Asakura Y, et al. Nanoarchitectonics of hollow covalent organic frameworks: synthesis and applications[J]. *ACS Nano*, 2023, 17(10): 8918-8934.
[40] Suleman S, Zhang Y, Qian Y Y, et al. Turning on singlet oxygen generation by outer-sphere microenvironment modulation in porphyrinic covalent organic frameworks for photocatalytic oxidation[J]. *Angewandte Chemie International Edition*, 2024, 63(2): e202314988.
[41] Zhan X N, Jin Y C, Qu C, et al. Synergistic strategy toward enhancing photosynthesizing reactive oxygen species of covalent organic frameworks[J]. *Advanced Functional Materials*, 2025, 35(8): 2415629.
[42] Li Z P, Jiao J Q, Fu W L, et al. Integration of perylene diimide into a covalent organic framework for photocatalytic oxidation [J]. *Angewandte Chemie International Edition*, 2024, 63(46): e202412977.
[43] Xing L B, Cheng K, Li H L, et al. Integrating two photochromics into one three-dimensional covalent organic framework for synergistically enhancing multiple photocatalytic oxidations[J]. *Angewandte Chemie International Edition*, 2025, 64(16): e202425668.

# 具有电子推拉效应的共价有机框架用于硫化物选择性光催化氧化

黄振轩，赵启新，蒋志强，曾　阳，申杰峰*，宣为民*
东华大学 先进纤维材料全国重点实验室，化学与化工学院，上海 201620

**摘　要：**硫化物的选择性有氧氧化有助于含亚砜的药物与农用化学品的高效生产。然而，传统的催化体系中硫化物易被过度氧化成砜，从而影响选择性。光催化已成为解决这一长期存在的选择性难题的变革性策略，并推动了对光催化材料的广泛探索。共价有机框架(covalent organic framework，COF)，由于其结构的可调性、可定制的光电特性及在光催化条件下的稳定性，成为硫化物光催化选择性有氧氧化的理想平台。本研究通过席夫碱缩合制备了两种 COF(TP-BPDA 和 BTT-BPDA)。光电化学试验表明，TP-BPDA 具有更显著的电子推拉效应，在硫化物选择性有氧氧化为亚砜方面表现出更好的光催化性能。此外，TP-BPDA 还具有广泛的底物通用性，基于捕获剂试验，本文提出了可能的反应机制。这项工作将为进一步开发利用电子推拉效应进行选择性有氧氧化的高效光催化剂提供指导。

**关键词：**共价有机框架；席夫碱缩合；亚砜；光催化